Scilight

Earth Sciences Perspectives

https://www.sciltp.com/journals/esp

Article

Study on the Influence of Structural Plane Dip Angle on Mechanical Properties of Surrounding Rock

Jia Zhao [1,2], Yanfeng Li [2,3,*], Guangzuo Feng [1,2], Lujun Wang [1,2], Baozuo Liu [1,2], Enyu Lu [1,2] and Liang Fang [4]

[1] China Railway No. 9 Group Co., Shenyang 110051, China
[2] School of Transportation and Geomatics Engineering, Shenyang Jianzhu University, Shenyang 110168, China
[3] School of Resources and Civil Engineering, Northeastern University, Shenyang 110819, China
[4] Undergraduate School, Jilin University, Changchun 130012, China
* Correspondence: lyfneu@126.com

How To Cite: Zhao, J.; Li, Y.; Feng, G.; et al. Study on the Influence of Structural Plane Dip Angle on Mechanical Properties of Surrounding Rock. *Earth Sciences Perspectives* **2025**, *1*(1), 2.

Received: 10 October 2025
Revised: 27 October 2025
Accepted: 29 October 2025
Published: 4 November 2025

Abstract: Deep mine roadways are highly susceptible to instability due to the combined effects of mining-induced and tectonic stresses, where localized weak planes play a critical role. This study investigates the influence of weak-plane dip angle on the mechanical behavior of surrounding rock and roadway stability, using the Xinli-Sanshandao fault zone as an engineering backdrop. Laboratory uniaxial compression tests were conducted on red sandstone specimens with weak planes at dip angles of 0°, 30°, and 60° to determine their mechanical parameters and failure modes. A three-dimensional elasto-plastic model in FLAC3D was then used to simulate scenarios with weak planes located above, below, or through the roadway. Results show that increasing dip angles reduce rock strength and peak strain while changing the failure mode from tensile to shear-dominated. Numerical simulations indicate that overhead weak planes mainly increase roof displacement, sub-roadway weak planes increase both roof and sidewall displacements, and through-going weak planes produce the most significant displacements and stress concentrations, leading to plastic deformation and the lowest roadway stability. These findings highlight that high-angle and through-going weak planes significantly compromise the load-bearing capacity of surrounding rock and present the greatest hazard to underground structures.

Keywords: weakening plane dip angle; mechanical behavior of surrounding rock; uniaxial compression test; numerical simulation; roadway stability

1. Introduction

With continued economic and social development, hard-rock mining activities have intensified. Large-scale mining operations severely disturb the original in-situ stress field of rock strata and generate substantial additional stresses. These stresses cause continuous and complex changes in the displacement and stress fields of the surrounding rock [1–6], ultimately leading to stope roadway instability.

During mineral extraction, instability often initiates in locally weakened zones of the surrounding rock—such as those with bedding planes, joints, and fractures. Influenced by internal and external factors, including rubble extrusion, slurry infiltration within weak zones, static loading from surrounding rock, and construction-induced vibrations, local fractures progressively expand. This further weakens the rock structure, potentially triggering large-scale instability and posing serious hazards [7–13].

Under mining disturbance, pillar instability often precedes roof collapse. Localized fracturing occurs first, forming weakened zones that expand gradually. The shear fracture zones in pillars and tensile fracture zones in

the roof represent such local weak areas, which extend and eventually connect, leading to pillar failure and roof caving [14–16]. Similarly, instability in sidewalls and other rock masses can induce localized weakening, causing rock spalling and sliding [17].

If the growth of these localized weak zones in the surrounding rock is not effectively controlled, overall roadway instability may result, potentially causing severe mining accidents. In extreme cases, such instability can extend to the ground surface, leading to subsidence and ecological damage.

Kumar [18] reported that rock masses containing macro- and meso-defects experience significant mechanical degradation due to internal damage evolution. Yu et al. [19] systematically revealed fracture zone formation and propagation in deep roadways under varying stress directions through field investigations, laboratory tests, monitoring, and numerical simulations. They highlighted the dominant role of fracture zones in rock deterioration and support failure, proposing control strategies to limit fracture initiation and extension. Li et al. [20] combined field study, theoretical analysis, physical modeling, and numerical simulation to analyze the asymmetric, time-dependent damage evolution in inclined rock-layer roadways in the Jinchuan mining area under in-situ stress and structural plane effects, clarifying key mechanisms of surrounding rock instability. Wang et al. [21] applied probabilistic methods to study the size effect and stress state in coal-rock strength weakening and proposed a quantitative approach to assess instability likelihood. Huang et al. [22] investigated mining-induced damage patterns in roadway surrounding rock through laboratory tests and developed a method to calculate weakening damage under load. Chen et al. [23] combined Split Hopkinson Pressure Bar (SHPB) tests with extended finite element simulations to systematically reveal how weak interlayers affect dynamic response and failure modes in rocks. They found that interlayers induce stress concentration and alter failure patterns, with tensile cracks increasing significantly with interlayer thickness. Günen [24] proposed a framework combining stacked auto-encoders and density-based clustering to estimate the orientation parameters of individual discontinuity sets from 3D point clouds, achieving classification accuracies exceeding 95% and orientation deviations within 5° of in situ measurements. In a related study, Günen [25] applied ensemble learning methods—including random forest, AdaBoost, and decision tree—along with explainable AI (SHAP analysis) to classify main discontinuity sets and derive plane orientation parameters via RANSAC. Both approaches were validated on real and synthetic datasets, demonstrating the robustness and practical applicability of machine learning techniques for identifying rock discontinuities, even in hazardous or difficult-to-access environments. These results provide experimental and numerical support for predicting rock mass instability under dynamic loads such as earthquakes and landslides.

Although existing studies confirm the significant impact of structural planes and weak interlayers on rock mechanical properties, targeted research on structural plane dip angles has distinct gaps. Most studies focus on the presence/absence of structural planes or their macroscopic effects, lacking systematic quantitative analysis of rock mechanical parameter evolution (e.g., uniaxial compressive strength, peak strain) under typical engineering dip angles (0°–60°) and failing to clarify dip angle-correlated quantitative relationships with key indicators. Research on the coupling effect of structural plane spatial position and dip angle is insufficient, with existing findings unable to fully reveal differential influences on surrounding rock displacement and stress distribution across different spatial positions (above the roof, below the floor, penetrating the roadway). Additionally, in-depth verification through integrated laboratory tests and numerical simulations is lacking, hindering accurate quantification of dip angle-dominated surrounding rock stability evolution and provision of targeted engineering parameter support.To address these gaps, this study takes the Xinli-Sanshandao fault zone as the engineering background, combining laboratory experiments and numerical simulations. It systematically investigates the effects of structural planes with three typical dip angles (0°, 30°, 60°) on red sandstone mechanical properties, clarifying quantitative relationships between dip angle and rock strength, strain, and failure modes. A 3D elastoplastic FLAC3D model is established to simulate structural planes in three spatial positions, revealing displacement and stress evolution laws of the roof and sidewalls under position-dip angle coupling. The innovations lie in: first quantifying mechanical parameter attenuation of red sandstone within 0°–60° and establishing a dip angle-stability correlation model; clarifying the position-dip angle coupling mechanism to fill the research gap in surrounding rock response under combined conditions; and providing precise parameter support for deep mine roadway stability control through test-simulation mutual verification.

2. Experimental Analysis of Dip Angle Effects on Surrounding Rock Mechanical Properties

2.1. Project Overview for the Study

The Xinli-Sanshandao fault zone, which serves as the ore-controlling structure in the mining area, constitutes the northeastern segment of the regional Sanshandao-Cangshang fault system. It comprises a main fault, associated feather faults in both the hanging wall and footwall, as well as several parallel faults branching from the footwall.

Using Line 11 as a dividing line, the fault zone can be divided into two distinct segments (Figure 1). This segment extends northeast from Line 11 to Line 187 in the southwest. It has a land-based exposure length of approximately 700 m and continues offshore south of Line 23. At the −165 m level, the fault is controlled by underground drilling as far as Line 171, while exploration drilling confirms its extension to Line 187. The total controlled length of this segment is about 2500 m, with a width ranging from 80 to 280 m. Stretching southwest from Line 11 to Line S56 via Line S8, this segment enters the sea at its northeastern end. It has a controlled length of roughly 1600 m and a width varying between 35 and 250 m. Although the fault's surface exposure lies outside the current exploration area, its deeper section extends into it.

The fault zone generally strikes northeast, the rose diagram of fracture dip angle distribution in the Xinli-Sanshandao Ore Section is shown in Figure 2 and exhibits the following structural characteristics: east of Line 11, the average strike is [insert value], whereas in the western Xinli segment (Lines 11–111), it strikes [insert value]. Near Line 147, the fault turns southward toward Line 159, then bends again toward Line 171. At shallow depths, the main fault dips northwest at angles of 70–80°, but it dips southeast at greater depths. Southwest of Line 171, the fault connects with the Cangshang fault zone, consistent with shallow seismic interpretations from 2002. Overall, the fault dips southeast at angles of 33–67° (typically 40–50°, averaging 46°). Only between Lines 159 and 171 does the shallow portion dip northwest at steep angles (70–80°); below −400 m, the dip reverts to southeast and becomes gentler. From northeast to southwest, the dip angle gradually steepens, forming gentle undulations both along strike and down dip, with strike variations being more pronounced than dip variations.The fault zone is developed within the Neoproterozoic Sinian Linglong sequence biotite granite and the Neoarchean Wutai-Fuping Malianzhuang and Qixia sequences, close to the inner belt of their contact zone. The hanging wall lies within 0–125 m of this contact.

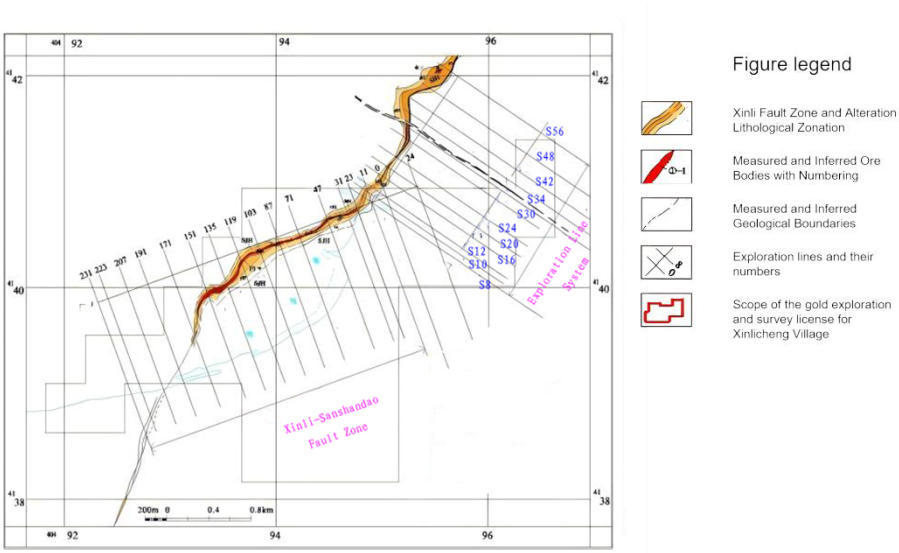

Figure 1. Distribution Map of Xinli-Sanshandao Fault Zone and Exploration Line System.

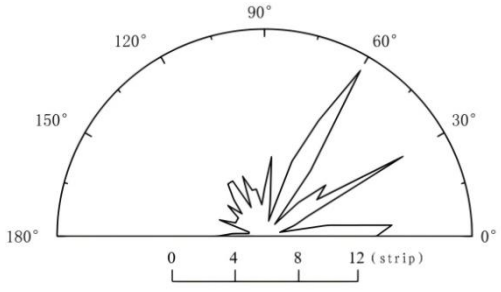

Figure 2. Rose Diagram of Fracture Dip Angle Distribution in Xinli-Sanshandao Ore Section.

2.2. Selection of Experimental Materials and Preparation of Specimens

According to the geological survey report of the Xinli-Sanshandao Fault Zone, the gold mining roadway in this area (located at a depth of 420–530 m) is situated within a complex rock system composed of multiple lithologies. The primary mineral constituents are quartz (60%), albite (17%), and calcite (10%). Due to site-

specific constraints, particularly the high-stress conditions in the deep mining environment, on-site drilling and sampling were not feasible. Since red sandstone is comparable to the on-site composite rock mass in terms of strength and stiffness, this study selects red sandstone with similar lithological characteristics as the test sample.Therefore, red sandstone with comparable lithological characteristics was selected as the test specimen for this study. Detailed data are provided in Tables 1 and 2.

Table 1. mineralogical composition.

Quartz	Calcite	Montmorillonite	Microcline	Albite	Illite	Chlorite	Hematite
59%	9%	7%	4%	15%	4%	1%	1%

Table 2. Basic Physical Parameters.

ρ_n g/cm³	ρ_d g/cm³	ρ_s g/cm³	w_s /%	n /%	V_p /(km/s)
2.38	2.341	2.432	3.89	9.59	2.874

ρ_n-Natural Density; ρ_d-Dry Density; ρ_s-Saturated Density; w_s-Saturated Moisture Content; n-Porosity; V_p-P-wave Velocity.

Thirty cylindrical specimens with a diameter of 50 mm and an initial length exceeding 104 mm were drilled and cored from intact red sandstone blocks. Following the standards outlined in the Test Code for Rock in Water Resources and Hydropower Engineering, the Standard for Test Methods of Engineering Rock Mass, and recommendations by the International Society for Rock Mechanics (ISRM), the specimens were processed to their final dimensions. They were first rough-ground to approximately 101 mm and then finely ground to a standard length of 100 ± 0.1 mm using an automatic precision surface grinder, resulting in standard cylindrical test pieces.

A total of 10 groups of specimens, each containing a persistent structural plane at dip angles β of 0°, 30°, and 60° (defined as the angle between the structural plane and the horizontal direction under major principal stress), were prepared using an AC 5-axis CNC waterjet cutting system. The preparation involved sectioning intact rock samples and subsequently bonding them together. The artificial structural planes were filled with a 2-mm-thick mixture of gypsum and uneven gravels, which simulated the localized weakening of surrounding rock while providing cohesion between sections. The flatness of the filled interface was controlled within a tolerance of ±0.02 mm. The specimen preparation process is illustrated in Figure 3. For comparison, 10 intact rock specimens of the same dimensions were also prepared as a control group.

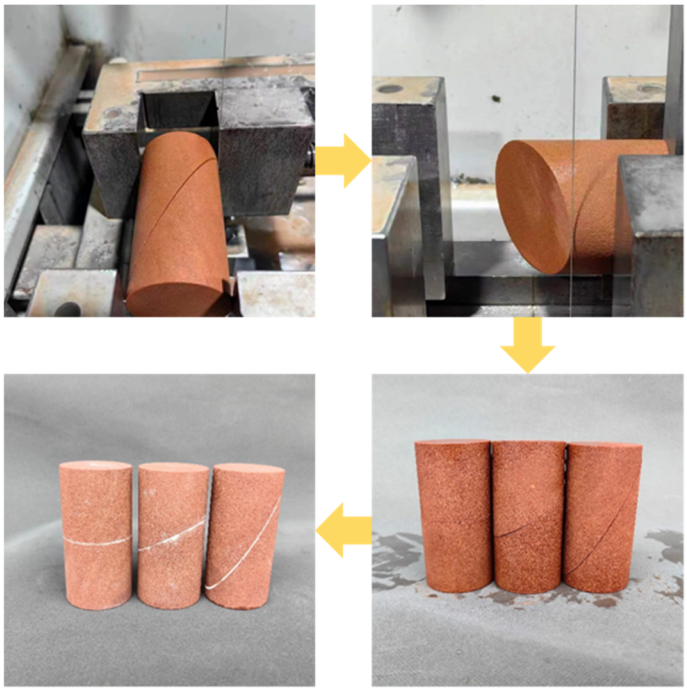

Figure 3. The process of preparing a structural surface inclination test specimen.

2.3. Uniaxial Compression Test Scheme and Result Analysis

The failure mode of rock specimens serves as the most direct manifestation and a critical characteristic of their failure mechanisms. The static uniaxial compressive strength of intact rock represents a fundamental mechanical parameter, essential for guiding the stability analysis of engineering rock masses and informing engineering design.

Extensive uniaxial compression tests on laboratory rock specimens have revealed a variety of failure types, which can be broadly categorized into five classes through classification and analogy [26]. Category A: Brittle ejection failure dominated by tension; Category B: Brittle tensile-shear failure; Category C: Wedge-splitting brittle failure; Category D: Flexible failure dominated by tension with concurrent compression; Category E: Flexible tensile failure and shear failure in soft rock.

Based on studies by J. C. Jaeger [27], You M.Q. et al. [28] and Huang D. et al. [29] on rock failure modes under uniaxial compression, the results dominated by shear failure can be further classified into three typical forms, as illustrated in Figure 4.

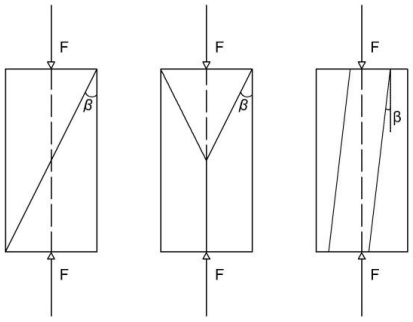

Figure 4. Results of uniaxial compressive tests based on shear failure Modes.

A 70-S18B2 testing machine (see Figure 5) was used to conduct uniaxial compression tests on a total of 40 specimens, including the intact ones. Figure 6 displays the failure modes of some specimens.

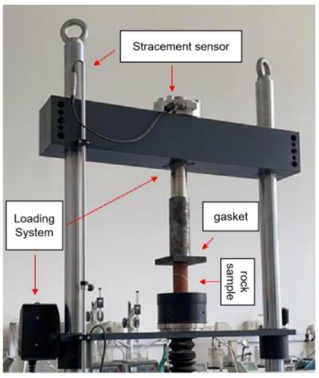

(**a**) 70-S18B2 Testing Machine

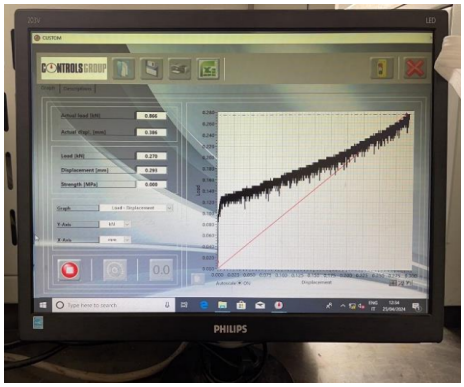

(**b**) Control Interface of the Testing Machine

Figure 5. Uniaxial Compression Test Equipment.

(**a**) Intact Specimen

(**b**) Specimen with 0° Dip Angle

(**c**) Specimen with 30° Dip Angle

(**d**) Specimen with 60° Dip Angle

Figure 6. Failure Diagrams of Partial Specimens.

Uniaxial compression tests were performed on intact specimens, the various mechanical parameters of the rock were obtained through experiments, with detailed data shown in Table 3. Since the selected similar materials are close to the actual engineering conditions and the fracture strike during failure is consistent with the actual situation, the obtained basic mechanical properties can provide effective support for the subsequent numerical simulation of surrounding rock roadways. The corresponding stress-strain curves are presented in Figure 7. During the axial compression test, for specimens with structural plane dip angles of 0° and 30°, the low-strength filling medium in the structural planes was compressed, deformed, and eventually crushed under loading. Angular fragments of varying sizes remained in the cracks between the two rock samples, resulting in uneven fragmentation of the filling medium. Smaller sharp-edged fragments exerted high pressure on the surfaces of the upper and lower rock masses during axial compression and could not be further crushed or compacted. Under loading, specimens with 0°and 30°dip angles failed to induce rolling friction among these fragments to allow the rock samples to slide along the structural plane; instead, these stronger small fragments were squeezed into the rock mass. This caused cracks to form in the relatively high-strength rock samples due to stress concentration, and continued loading led to the gradual propagation and connection of these cracks with existing rock mass fractures until complete failure occurred. In contrast, during the loading process of the 60°dip angle specimen, the filling medium in the structural plane underwent compression, deformation, and shear dislocation, which prevented the rock mass from fully exerting its bearing capacity. Sufficient external load disrupted the original equilibrium state of the rock mass, causing the sample to slide along the structural plane and resulting in a significant weakening of the specimen's strength.

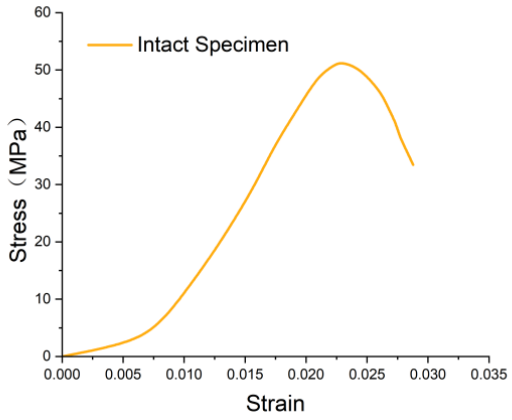

Figure 7. Stress-Strain Curve for Complete Cylindrical Specimens.

Table 3. Basic Mechanical Parameters of Intact Red Sandstone Specimens.

E (GPa)	$\boldsymbol{\sigma_c}$ **(MPa)**	$\boldsymbol{\varphi}$ **(°)**	ν
6.524	51.54	45.11	0.25

The basic mechanical parameters of the remaining 30 specimens were determined using Equations (1)–(3). The stress–strain curves (Figure 8) indicate that the rock strength decreases significantly with increasing dip angle of the structural plane. Compared to the intact specimens, the uniaxial compressive strength dropped by 8.58–31.90 MPa (16.68–61.97%), while the failure strain decreased by 0.007–0.022 (22.33–73.33%). Compared with intact specimens, for specimens weakened by structural plane dip angles, the fragments within their filling materials increase the paths and channels for crack propagation in the rock samples, resulting in a progressive failure process dominated by the failure of the rock sample itself under the influence of weakening. It can thus be seen that the occurrence of instability is not only related to the bearing limit of the rock mass's own mechanical properties, but also that weakening reduces the strength of the rock mass.

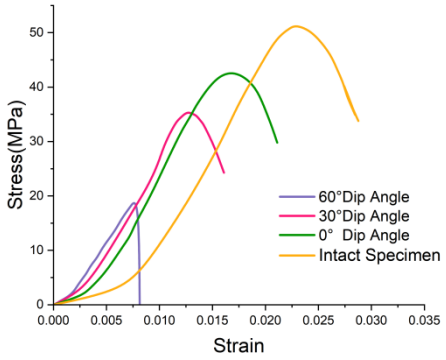

Figure 8. Stress-Strain Relationship Curves for Specimens with Various Dip Angles and Intact Specimens.

3. Numerical Simulation and Result Analysis

3.1. Numerical Simulation Model

Numerical simulations were performed in FLAC3D to evaluate the effect of structural weakening planes (at dip angles of 0°, 30°, and 60°) on the mechanical behavior of the surrounding rock. According to the actual engineering conditions, the actual mining situation is simplified into a three-dimensional plane finite difference elastoplastic constitutive model, with the numerical calculation section selected perpendicular to the strike of the mining area. The gold-bearing layers and soil layers in each roadway are in conformable contact, and the interior of the rock layers is treated as a continuous medium. Based on the on-site inspection report, the physical and mechanical parameters of each rock layer in the key stratum are selected, and the rock mass parameters from bottom to top are shown in Table 4.

Table 4. Numerical simulation of rock parameters.

Rock Stratum	ρ (kg/m^3)	K (GPa)	G (GPa)	T (MPa)	c (MPa)	φ (°)
Upper Surrounding Rock	2700	12.3	8.5	0.36	2.65	45
Weakened Layer	1902	7.73	4.5	0.47	0.3	21
Roof	1414	2.449	0.64	0.6	0.5	14
Ore Body	1414	2.449	0.64	0.6	0.5	14
Floor	1414	2.449	0.64	0.6	0.5	14
Lower Surrounding Rock	2700	12.3	8.5	0.36	2.65	45

The gold ore body has an average thickness of 3 m, and the most widely distributed dip angles of the weakened fissures in the roof of the ore body are 0°, 30°, and 60°. Mining advances gradually along the strike direction of the ore body. At the location of the main haulage roadway, a fault with a certain dip angle cuts through the roof of the roadway. The mining depth of the ore body ranges from 420 m to 530 m. In the final numerical model, the average mining depth is set at 500 m, the roadway excavation width is 6 m, the ore body thickness is 3 m, and the model length is 50 m, as shown in Figure 9.

The upper surface of the numerical model adopts a free-surface boundary condition, meaning no constraints are applied and the top is allowed to deform freely. This setting better reflects actual conditions, as in real geological or mining environments, the upper surface is typically unconstrained. The free-surface condition enables a more realistic simulation of in-situ stress release and deformation behavior.

Based on the in-situ stress conditions corresponding to a burial depth of 500 m, initial vertical and horizontal stresses are applied to the upper surface. The lateral boundaries are horizontally constrained, while the bottom boundary is fully fixed. The excavation area (stope) is located at the center of the model. To minimize boundary effects on the results, the dimensions of the numerical model are set to be approximately 3–5 times larger than the excavation area. The overall model is a rectangular block with dimensions of 50 m × 50 m × 27 m.

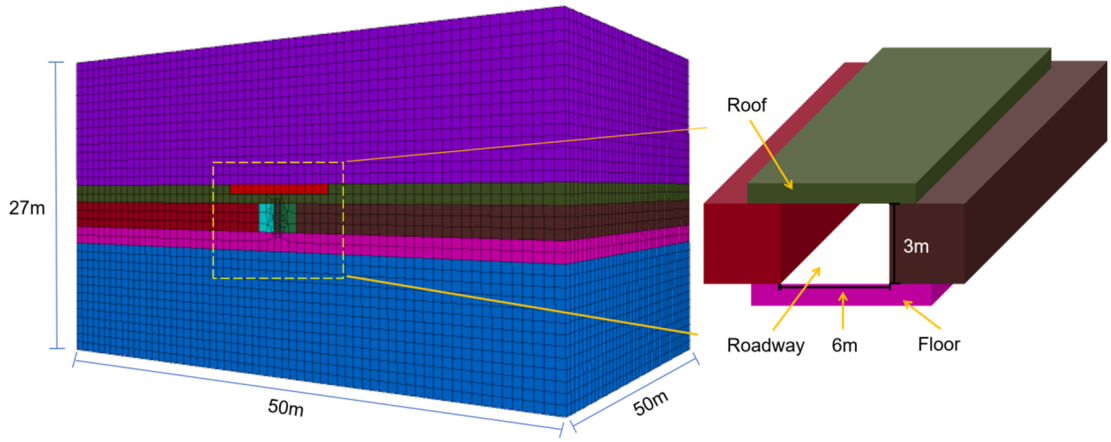

(**a**) Numerical Analysis Model of Roadway Surrounding Rock

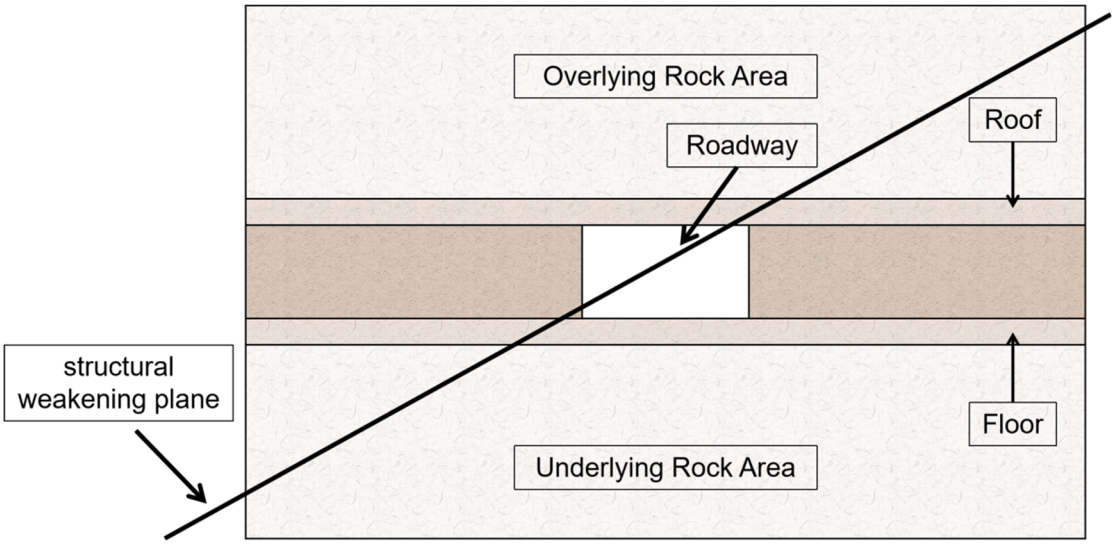

(**b**) Plan View of Roadway Surrounding Rock

Figure 9. Roadway Model Diagram.

The configurations of the structural weakening planes for the three dip angles (0°, 30°, and 60°) are presented in Figure 10. The models corresponding to the three scenarios for the 0°, 30°, and 60° planes are shown in subplots (a–c), (d–f), and (g–i), respectively.

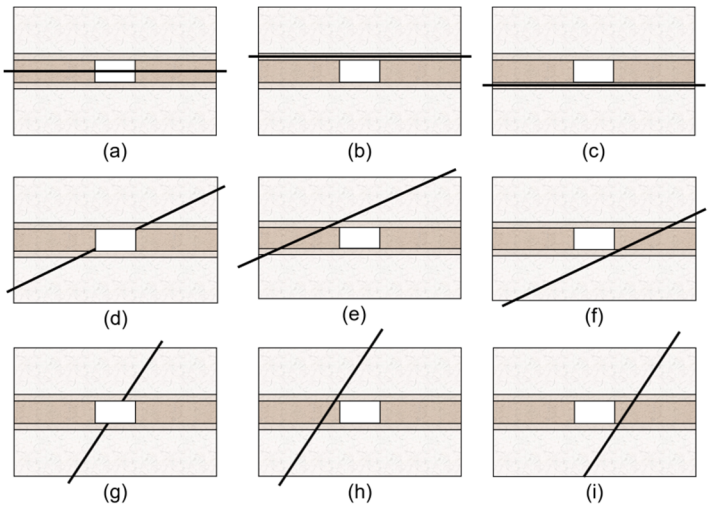

Figure 10. Diagram of Structural Weakening Plane Positions ((**a**–**c**): The structural weakening planes at 0°; (**d**–**f**): The structural weakening planes at:30°; (**g**–**i**): The structural weakening planes at 60°).

3.2. Analysis of Roof and Right Sidewall Displacements

The numerical simulation was conducted at a depth of 500 m, corresponding to the typical mining depth (420–530 m) of the gold mine, to analyze the deformation of surrounding rock induced by roadway excavation beneath a weakened fracture zone. Deformation monitoring points were installed on the roof and sidewalls to record displacement data. Figure 11 shows the roadway displacement curves and the maximum displacement profile for the case where the structural weakening plane is located above the roadway.

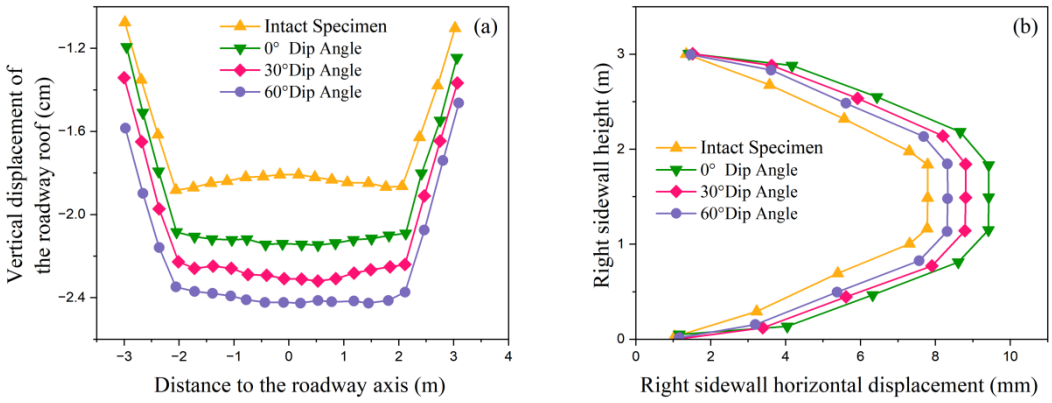

Figure 11. Roof and Right Sidewall Displacements under an Overhead Structural Weakening Plane: (**a**) Roof Displacement, and (**b**) Right Sidewall Displacement.

The vertical displacement of the roadway roof increases by 5.43% to 13.18% as the dip angle of the weakening plane rises, reaching maximum values of −21 mm, −22 mm, and −24.5 mm at 0°, 30°, and 60°, respectively. These results reflect a clear degradation in the bearing capacity of the central roof region. In contrast, sidewall displacements decrease with increasing dip angle, showing a reduction of 6.38% to 11.71%. The maximum sidewall displacements recorded at the center of the right sidewall are −9.42 mm, −8.79 mm, and −8.31 mm for the corresponding angles. Overall, roof deformation exhibits greater sensitivity to the presence of the weakening plane. The maximum roof displacements exceed those in intact rock by 16% to 33%, while the right sidewall shows a comparatively smaller increase of 8% to 22%.

When the weakening plane is located beneath the roadway (Figure 12), the vertical displacement of the roof increases with the dip angle, showing a growth of 9.52% to 20.83% and reaching values of −19 mm, −21 mm, and −24 mm at 0°, 30°, and 60°, respectively. The horizontal displacement of the sidewall also increases with the dip angle, rising by 6.61% to 11.32%, with corresponding maximum values of −9.42 mm, −9.91 mm, and −10.65 mm.

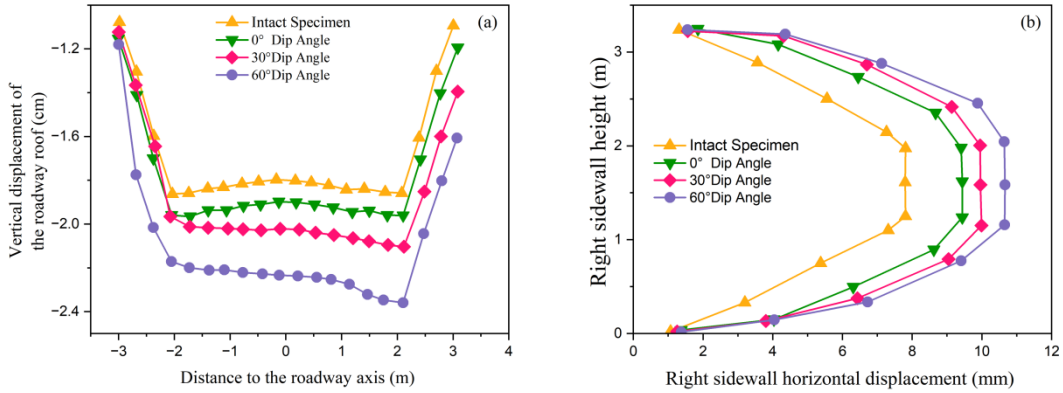

Figure 12. Roof and right sidewall displacements under an underlying weakening plane ((**a**): Vertical displacement curve graph of the roof slab in the roadway; (**b**): Horizontal displacement curve graph of the roadway side).

The deformation of the roadway intensifies as the weakening plane inclines toward the right sidewall. Compared to the intact rock model, the roof displacement increases by 6% to 33%, while the sidewall displacement increases by 4% to 30%.

When the weakening plane penetrates the roadway (Figure 13), both roof and sidewall displacements increase markedly. Compared to the scenarios with overhead or underlying weakening planes, roof displacement rises by

43.24–74.44%, and sidewall displacement increases by 28.45–31.88%. Relative to the intact rock model, the roof displacement grows by 50.27–89.66% and the sidewall displacement by 32.76–44.21% across dip angles of 0°, 30°, and 60°. When the weakening plane penetrates the roadway, the mechanical behavior of the roadway rock mass is most consistent with that observed in the experiments. As the dip angle increases, combined tensile failure occurs, and the bearing capacity of the surrounding rock mass decreases significantly. Under this through-going weakening condition, both roof and sidewall displacements exceed the safety threshold, indicating that the surrounding rock has entered a plastic state. Continuous stress monitoring is therefore recommended to evaluate the ultimate bearing capacity of the roof.

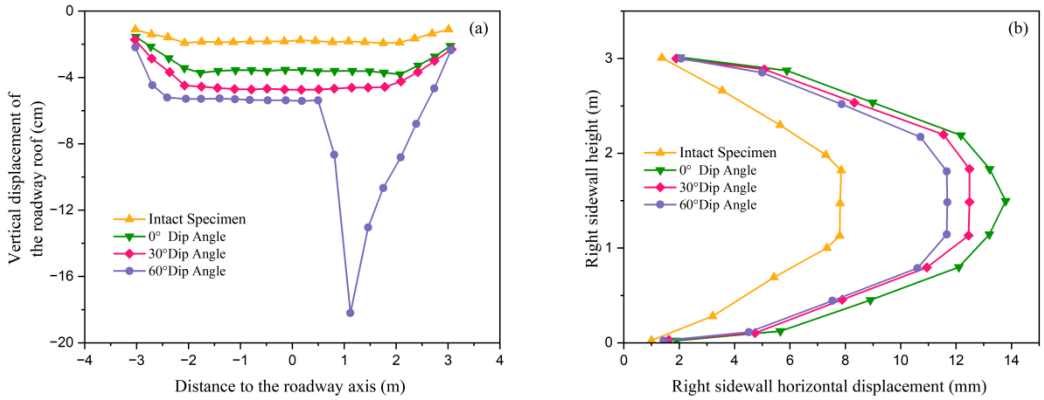

Figure 13. Roof and right sidewall displacements under a through-going weakening plane ((**a**): Vertical displacement curve graph of the roof slab in the roadway; (**b**): Horizontal displacement curve graph of the roadway side).

3.3. Analysis of the Roof and Right Sidewall Stress

3.3.1. Stress Analysis of the Roadway Roof

In this subsection, compressive and tensile stresses are defined as positive and negative values, respectively. As the lateral position changes, the roof stress state transitions from tension to compression and back to tension. In the case of intact rock, the vertical stress distribution across the roof approximates a relatively symmetric and smooth arch-shaped curve. Tensile stress is more pronounced on both sides of the roadway, while the central region transitions into compression, peaking at 1.01 MPa at the centerline. In the absence of a weakening plane, stress concentration occurs primarily along both sides of the roadway, whereas the stress distribution near the roof center remains uniform—indicating satisfactory stability. The corresponding roof stress curve is shown in Figure 14.

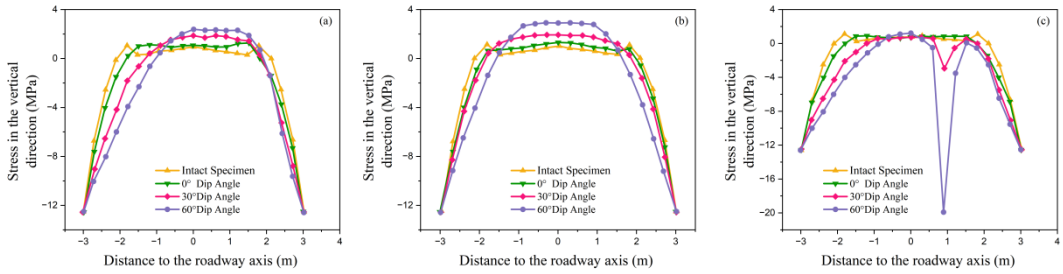

Figure 14. Roof stress distribution under varying positions and dip angles of weakening planes: (**a**) Roof stress curve under an overhead structural weakening plane; (**b**) Roof stress curve under an underlying structural weakening plane and (**c**) Roof stress curve under a through-going structural weakening plane.

As the dip angle of the structural plane increases from 0° to 60°, the vertical stress distribution in the roadway roof becomes increasingly non-uniform, with continuous growth in peak stress values and a corresponding decline in the bearing capacity and stability of the rock mass. Furthermore, the dominant factors driving stress variation and associated displacement responses vary considerably with dip angle.

Figure 13a shows the roof stress distribution when the structural weakening plane is located above the roadway. The presence of the weakening plane significantly alters the vertical stress profile, shifting the stress concentration zone toward the right side of the roadway. At 0°, the distribution remains close to that of intact rock, although stresses on both sides decrease by approximately 10.05%, and the peak compressive stress at the

centerline reaches 1.1 MPa. As the dip angle increases, the distribution grows more asymmetric. At 30°, a clear asymmetry emerges, with the centerline peak stress rising to 2.0 MPa. At 60°, the weakening effect intensifies, and the peak stress at the centerline reaches 2.4 MPa—an increase of 118.2% and 20% compared to the values at 0° and 30°, respectively.

Figure 13b presents the roof stress distribution for the case where the weakening plane lies beneath the roadway. Although the structural plane reduces the overall bearing capacity, the greater distance from the roof results in a nearly symmetric stress curve. As the dip angle increases, the stress peak shifts toward the centerline and rises progressively to 1.3 MPa, 1.8 MPa, and 2.9 MPa. More pronounced stress reductions occur at positions ±2–3 m from the centerline. At a dip angle of 60°, the peak roof stress is 123.1% and 61.1% higher than that at 0° and 30°, respectively.

As shown in Figure 13c, when the weakening plane penetrates the roadway, the roof stress distribution assumes an "M-shaped" profile. At dip angles of 30° and 60°, distinct tensile stress concentrations occur at 0.9 m from the centerline—corresponding to the intersection of the weakening plane and the roof—reaching values of –3.0 MPa and –19.87 MPa, respectively. These extreme values deviate markedly from the intact rock curve, reflecting intense local tensile stresses. With increasing dip angle, the inclination between the weakening plane and the principal stress direction increases, leading to asymmetric stress redistribution and higher tensile stresses sustained by the roof.

3.3.2. Stress Analysis of the Right Roadway Sidewall

Figure 15 presents the right sidewall stress distribution under varying positions and dip angles of weakening. The stress variation at a height of 3 m on the right sidewall (i.e., the roadway roof position) is primarily influenced by the spatial distance between the weakened zone and the sidewall, with distinctly different responses under varying positions of the weakening plane.

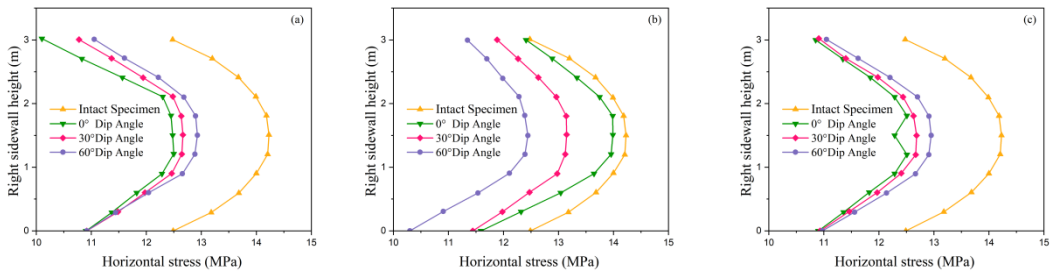

Figure 15. Right sidewall stress distribution under varying positions and dip angles of weakening planes: (**a**) Horizontal stress curve of the right sidewall under an overhead structural weakening plane; (**b**) Horizontal stress curve of the right sidewall under an underlying structural weakening plane and (**c**) Horizontal stress curve of the right sidewall under a through-going structural weakening plane.

At the right sidewall roof: When the weakening plane is located above the roadway, an increase in dip angle enlarges the distance to the sidewall, which reduces interference and raises the horizontal stress by 2.72–8.85%. Nonetheless, these values remain 9.15–11.97% below those in intact rock; For sub-roadway weakening, the horizontal stress stays below the intact rock level without a clear correlation to dip angle, while the vertical stress increases by 0.6 MPa (+5.6%) at 1 m from the sidewall due to stress transfer from the weakened floor; Under through-going weakening, the horizontal stress shows a symmetric distribution and remains lower than in intact rock, whereas the vertical stress exhibits the most significant increase, rising by 0.9 MPa (+7.5%) at 1 m.

At the right sidewall centerline: With overhead weakening, horizontal stress slightly increases with dip angle (12.5–12.9 MPa), though still 9.15–11.97% below the intact rock reference; this reduction diminishes as the dip angle increases; Under sub-roadway weakening, horizontal stress decreases with dip angle from 13.2 MPa to 11.6 MPa, corresponding to a reduction of 7.04–18.31%, with the most pronounced effect at 60°; In the through-going weakening scenario, horizontal stress remains symmetrically distributed, with peak values of 12.2–12.9 MPa—8.45–14.08% lower than intact rock. A localized stress release is uniquely observed at a dip angle of 0°.

At the right sidewall floor: Stresses are most significantly influenced by sub-roadway weakening. As the dip angle increases, interference intensifies and horizontal stress decreases. Stresses at 0° and 30° are 11.21% and 9.65% higher than at 60°, respectively, yet remain 7.04–18.31% below the intact rock level overall; Under both overhead and through-going weakening, horizontal stress also remains below the intact rock level, displaying an asymmetric distribution in the former and a symmetric curve in the latter; The increase in vertical stress is less

pronounced than in the sub-roadway case; however, through-going weakening still leads to a greater increase (+7.5%) compared to overhead weakening (+3%), indicating its stronger overall impact on sidewall stress.

4. Conclusions

Based on integrated laboratory experiments and numerical simulations, this study systematically examined the influence of structural plane dip angle and spatial position on the mechanical response of surrounding rock. The main conclusions are summarized as follows:

(1) The dip angle of structural planes exerts a decisive influence on the mechanical behavior of rock masses. As the dip angle increases from 0° to 60°, the mechanical performance of red sandstone specimens deteriorates significantly: the uniaxial compressive strength decreases by 16.68–61.97% (corresponding to 8.58–31.9 MPa), the failure strain declines by 22.33–73.33%, and the rock exhibits more pronounced brittleness. The failure mode evolves from tensile splitting in intact rock to shear-dominated failure, demonstrating that high-angle structural planes markedly weaken the load-bearing capacity of the rock mass.In deep mining and underground excavation design, structural planes with large dip angles (>45°) should be regarded as potential failure zones, where targeted reinforcement or pre-grouting treatment is recommended to ensure stability.

(2) The deformation behavior of roadways is jointly controlled by the location and dip angle of the weakening plane. When the weakening plane is located above the roadway, roof displacement increases with dip angle, reaching 16%, 22%, and 33% higher than those of intact rock at 0°, 30°, and 60°, respectively (2.6 mm, 3.6 mm, and 5.6 mm). In contrast, right sidewall displacement decreases with dip angle (by 22%, 14%, and 8%), as the increasing inclination enlarges the distance between the weakening zone and the sidewall, reducing its influence. When the weakening plane lies beneath the roadway, both roof and sidewall displacements increase with dip angle, peaking at 33% and 30% above intact rock values at 60°. The most severe deformation occurs under through-going weakening, where roof displacement reaches –180 mm (an 89.66% increase) and sidewall displacement rises by 32.76%. In this case, the surrounding rock enters a plastic state, leading to tensile–shear composite failure and the lowest level of roadway stability.For roadway sections affected by high-dip or through-going weakening planes, comprehensive reinforcement of both the roof and sidewalls is necessary. Support systems should be optimized to control excessive deformation and prevent tensile–shear coupled failures.

(3) Weakening conditions significantly modify the stress redistribution patterns surrounding the roadway. In intact rock, the roof stress exhibits a symmetric arch-shaped distribution. The introduction of a weakening plane disrupts this uniformity, and as the dip angle increases, localized tensile and compressive stress concentrations become more pronounced. Under through-going weakening at 60°, the tensile stress at the roof centerline reaches –19.87 MPa, indicating severe obstruction of stress transfer. For the sidewall, the horizontal stress peak at the mid-height (1.5 m) is 14.2 MPa in intact rock but decreases by 7.04–18.31% under all weakening scenarios, with the greatest reduction observed when the weakening plane lies beneath the roadway. Conversely, vertical stress increases under weakening; through-going weakening raises the vertical stress at 1 m by 0.9 MPa (+7.5%), implying an elevated risk of compressive failure in the sidewall. The redistribution of stresses under weakened conditions highlights the necessity of localized reinforcement in stress concentration zones, particularly at the roof centerline and sidewall toe, to mitigate tensile and compressive failure risks and ensure long-term roadway stability. Due to project constraints, this study was conducted solely based on red sandstone, which presents certain limitations; therefore, the conclusions may not be applicable to other lithologies.

Author Contributions

J.Z.: conceptualization, methodology, software; Y.L.: data curation, writing—original draft preparation; G.F.: visualization, investigation; L.W.: supervision; B.L.: software, validation; E.L.: writing—reviewing and editing; L.F.: investigation. All authors have read and agreed to the published version of the manuscript.

Funding

This research received no external funding.

Institutional Review Board Statement

The study did not involve humans or animals.

Informed Consent Statement

The study did not involve humans.

Data Availability Statement

All the data involved in this article are indicated in the paper.

Conflicts of Interest

The authors declare no conflict of interest.

Use of AI and AI-Assisted Technologies

No AI tools were utilized for this paper.

References

1. Wang, Y.C.; Jing, H.W.; Chen, K.F.; et al. Study on the Distribution Law and Spatial Zoning of In-situ Stress in Pingdingshan Mining Area. *Chin. J. Rock Mech. Eng.* **2014**, *33*, 2620–2627.
2. Peng, C.D. Review on Latest Research Progress of Mine Pressure and Strata Control. *J. China Univ. Min. Technol.* **2015**, *44*, 1–8.
3. Li, T.; Gong, H.; Xu, G. Study on the Influence of In Situ Stress Distribution on the Stability of Roadway Surrounding Rock. *Adv. Civ. Eng.* **2021**, *2021*, 3570523.
4. Li, J.; Wang, Z.-F.; Wang, Y.; et al. Analysis and countermeasures of large deformation of Deep-buried tunnel excavated in layered rock strata: A case Study. *Eng. Fail. Anal.* **2023**, *146*, 107057.
5. Sun, X.; Jiang, M.; Miao, C.; et al. Study on large deformation and failure mechanism of deep buried stratified slate tunnel and control strategy of high constant resistance anchor Cable. *Eng. Fail. Anal.* **2023**, *144*, 106953.
6. Sun, G.Z.; Huang, Y.F. Principle of Surrounding Rock Weakening and Its Analysis. *Chin. J. Geosci.* **1989**, *4*, 385–392.
7. Feng, X.T.; Yang, C.X.; Kong, R.; et al. Excavation induced deep hard rock fracturing: Methodology and applications. *J. Rock Mech. Geotech. Eng.* **2022**, *14*, 1–34.
8. Wagner, H. Deep mining: A rock engineering challenge. *Rock Mech. Rock Eng.* **2019**, *52*, 1417–1446.
9. Wu, J.X. Experimental Study on Hydraulic Fracturing Controlling Initial Roof Caving in Fully Mechanized Top-Coal Caving Face. *J. Coal Sci. Technol.* **2016**, *44*, 91–95.
10. Nayebzadeh, A.; Wang, Y.; Tabkhi, H.; et al. Cavitation behind a circular micro pillar. *Int. J. Multiph. Flow* **2018**, *98*, 67–78.
11. Zhao, J.; Tan, Z.; Li, Q.; et al. Characteristics and mechanism of large deformation of squeezing tunnel in phyllite Stratum. *Can. Geotech. J.* **2024**, *61*, 59–74.
12. Deng, H.-S.; Fu, H.-L.; Shi, Y.; et al. Countermeasures against large deformation of Deep-buried soft rock tunnels in areas with high geostress: A case Study. *Tunn. Undergr. Space Technol.* **2022**, *119*, 104238.
13. Liu, D.; Huang, S.; Ding, X.; et al. Characteristics and Mechanism of Large Deformation of Tunnels in Tertiary Soft Rock: A Case Study. *Buildings* **2023**, *13*, 2262.
14. Wang, J.A.; Shang, X.C.; Liu, H.; et al. Study on Fracture Mechanism and Catastrophic Collapse of Hard Roof in Goaf. *J. China Coal Soc.* **2008**, *33*, 850–855.
15. Wang, C.W.; Jiang, F.X.; Wang, P.; et al. Distribution Characteristics of Microseismic Events and Mechanical Mechanism of Rock Burst Induced by Coal Pillar. *J. China Coal Soc.* **2009**, *34*, 1169–1173.
16. Chen, L.; Xi, B.; Zhao, N.; et al. Large Deformation Mechanism and Support Countermeasures of Deep-Buried Soft Rock Tunnels Under High Geostress State. *Buildings* **2025**, *15*, 704.
17. Liu, Q.S.; Lu, X.L. Study on Nonlinear Large Deformation of Fractured Surrounding Rock and Support Countermeasures in Deep Coal Mine Roadways. *Chin. J. Geomech.* **2010**, *31*, 3273–3279.
18. Kumar, R.; Das, A.J.; Mandal, P.K.; et al. Probabilistic stability analysis of failed and stable cases of coal pillars. *Int. J. Rock Mech. Min. Sci.* **2021**, *144*, 104810.
19. Yu, X.; Yang, Y.; Li, X.; et al. Cracking formation and evolution in surrounding rock of a deep fractured rock mass roadway: A study of the 790-m level segment engineering at the Jinchuan Mine, China. *Eng. Geol.* **2024**, *331*, 107431.
20. Li, G.; Sun, Q.; Ma, F.; et al. Damage evolution mechanism and deformation failure properties of a roadway in deep inclined rock Strata. *Eng. Fail. Anal.* **2023**, *143*, 106820.
21. Wang, F.; Feng, X.-T.; Zhou, Y.; et al. Deformation and Cracking Evolution Mechanism of Surrounding Rock in Deep Clastic Rock Tunnels: A Scaled-Down Excavation Experimental Study. *Rock Mech. Rock Eng.* **2025**, *58*, 7857–7877.
22. Huang, F.; Zhu, H.; Xu, Q.; et al. The effect of weak interlayer on the failure pattern of rock mass around tunnel–Scaled model tests and numerical Analysis. *Tunn. Undergr. Space Technol.* **2013**, *35*, 207–218.
23. Chen, J.; Gu, S.; Zhou, X. The effects of weak interlayers on the dynamic mechanical properties and failure behaviours of rocks: A combined numerical and experimental Analysis. *Int. J. Impact Eng.* **2023**, *180*, 104680.

24. Günen, M.A.; Aliyazıcıoğlu, Ş. Discontinuities identification from rock outcrop using auto-encoder and point clouds. *Bull Eng Geol Env.* **2025**, *84*, 418.
25. Günen, M.A. Explainable artificial intelligence for rock discontinuity detection from point cloud with ensemble methods. *J. Rock Mech. Geotech. Eng.* **2025**, *in press.*
26. Guo, Z. *Practical Rock Mass Mechanics*; Seismological Press: Beijing, China, 1996.
27. Jaeger, J.C. Shear failure of anisotropic rocks. *Geol. Mag.* **1960**, *97*, 65–72.
28. You, M.Q.; Hua, A.Z. Failure modes and bearing capacity reduction of rock specimens under uniaxial compression. *Chin. J. Rock Mech. Eng.* **1998**, *17*, 292–296.
29. Huang, D.; Huang, R.Q.; Zhang, Y.X. Experimental study of static loading rate effect and energy mechanism of mechanical properties of coarse marble under uniaxial compression. *Chin. J. Rock Mech. Eng.* **2012**, *31*, 245–255.